Journal of Fluids and Structures 118 (2023) 103836

Contents lists available at ScienceDirect

Journal of Fluids and Structures

journal homepage: www.elsevier.com/locate/jfs

Study of unsteady aerodynamic performance of a high-speed train entering a double-track tunnel under crosswind conditions

Jianjun Luo [a,b], Lei Wang [a,b,*], Suying Shang [c], Feilong Li [a,b], Dilong Guo [d,e], Liping Gao [a,b], Dengke Wang [a,b]

[a] School of Civil Engineering, Beijing Jiaotong University, Beijing 100044, China
[b] Key Laboratory of Urban Underground Engineering of the Ministry of Education, Beijing Jiaotong University, Beijing 100044, China
[c] Beijing Xinqiao Technology Development Co., Ltd., Beijing, 100088, China
[d] Key Laboratory of Mechanics in Fluid Solid Coupling System, Institute of Mechanics, Chinese Academy of Sciences, Beijing 100190, China
[e] Institute of Mechanics, Chinese Academy of Sciences, Beijing, 100190, China

ARTICLE INFO

Article history:
Received 20 August 2021
Received in revised form 2 August 2022
Accepted 23 January 2023
Available online 1 February 2023

Keywords:
Aerodynamic performance
Flow structures
High-speed train
Crosswinds
Railway tunnel
Transient pressure

ABSTRACT

Significant variation exists in the aerodynamic performances of high-speed trains (HSTs) traveling in different infrastructure scenarios. When high-speed trains travel from one infrastructure scenario to another, the aerodynamic loads acting on the trains change significantly. To investigate the safety as a HST enters a tunnel under crosswind conditions, the unsteady aerodynamic performance of the HST and the flow structures around the train were numerically studied. The results demonstrated that the flow field and the pressure field were symmetrically distributed under conditions with no crosswind, while the distribution of the flow field and the pressure field were clearly asymmetric when crosswinds were present at the tunnel entrance. Furthermore, the flow structures near the train and the pressure distributed on the train surfaces outside the tunnel were most severely affected by the presence of crosswinds. Vortex structures appeared on the windward side surface of the train inside the tunnel and on the leeward side surface of the train outside the tunnel during the entrance of the train into the tunnel. Due to the sudden changes in the flow and the pressure as the train entered the tunnel, the aerodynamic loads changed drastically, and the variations of each vehicle were different, resulting in complex dynamic responses, including lateral vibrations and pitching movement. In particular, the aerodynamic performance of the rear vehicle was the worst as the train entered the tunnel when no crosswind conditions existed, while the head vehicle was the most negatively affected for safe operation of the HST when strong crosswinds were present at the tunnel entrance.

1. Introduction

As a train is subjected to a strong crosswind, the resultant speed of the wind relative to the train maybe very high, causing the train to experience drastic aerodynamic forces and moments that can result in overturning or a derailment.

* Correspondence to: Key Laboratory of Urban Underground Engineering of the Ministry of Education, Beijing Jiaotong University, No. 3 Shangyuancun, Haidian District, Beijing, 100044, China.
E-mail address: 17115298@bjtu.edu.cn (L. Wang).

https://doi.org/10.1016/j.jfluidstructs.2023.103836
0889-9746/

Currently, trains with modern designs are lighter but travel faster than those with old designs. The combination of higher speeds and lower train weights increases the risk of accidents induced by the wind. This is because it is only the weight of the train that counteracts the aerodynamic forces acting on it. Crosswinds have become one of the most significant factors affecting the safety of the trains (Cooper, 1980; Baker, 2009; Zhuang and Lu, 2015). In the past several decades, many train accidents induced by crosswinds have occurred in numerous countries (Cooper, 1980; Baker, 2010; Zhuang and Lu, 2015; Sun et al., 2019; Hemida and Krajnović, 2010; Suzuki et al., 2003; Cooper, 1981) such as New Zealand, the United Kingdom, Japan, and China. The effects of crosswinds on the safe operation of trains have been a widespread concern around the world.

To investigate the aerodynamic performance of HSTs under crosswind conditions, a number of researchers focused on the impact of crosswind on train on aerodynamic performances. Guo et al. (2019) examined the aerodynamic behavior of a single-marshalling train and two single-marshalling trains under sidewind with small yaw angle (10°) by IDDES method using 1:8 scale models. They found that the coupling zone affected the aerodynamic forces acting on the train. Yao et al. (2014) and Yao et al. (2016) investigated how the nose length and the head shape affect the aerodynamic performances of HSTs. Niu et al. (2018) investigated the impact of crosswind on trains of different lengths by computational fluid dynamics (CFD). Furthermore, the aerodynamic characteristics under crosswinds are not only related to HSTs and crosswinds, but they are also closely associated with the infrastructure types along the railway line. Different infrastructures, such as viaducts, embankments, and tunnels, may exist along high-speed railway lines (Chen et al., 2020).

Currently, researchers are mainly focused on the crosswind effects as HSTs travel in a single infrastructure scenario, e.g., level ground (Rocchi et al., 2018; Niu et al., 2017a), embankments (Baker, 1985; Guo et al., 2020; Tomasini et al., 2014; Diedrichs et al., 2007; Ali et al., 2016), cuttings (Zhang et al., 2015; Liu et al., 2018), bridges (Montenegro et al., 2020; Yao et al., 2020). Furthermore, Chen et al. (2020), Wang et al. (2020), Suzuki et al. (2003), and Cheli et al. (2010) analyzed the aerodynamic performance of trains running under diverse environmental conditions. The results showed that the aerodynamic behaviors of the trains were affected significantly by the infrastructures along the railway lines. However, when trains pass through sections connecting different infrastructures under strong crosswinds, the aerodynamic performances of the trains have not been considered.

By the end of 2020, the operating range of China's high-speed railway system reached 38,000 km. The Sichuan–Tibet Railway, which is under construction, is one of the most important main railway lines in southwestern China. The length of the newly built main line from Ya'an to Linzhi is 1011 km, and the total length of the bridges and tunnels is 965.74 km, which account for 95.76% of the railway. In particular, 114.22 km containing 93 bridges and 851.48 km including 72 tunnels will be newly built. The percentages of bridges and tunnels over the total length of the railway line are 11.33% and 84.43%, respectively. Among the tunnels, 15 are longer than 20 km, and seven are longer than 30 km. The Yigong tunnel is the longest along the railway line, which is 42.486 km long. Consequently, scenarios such as a tunnel connecting to a bridge or a tunnel connecting to level ground will be more common during operation. Therefore, to analyze the aerodynamic performances of trains under crosswinds, it is crucial to consider the impacts of variations of the infrastructure scenarios.

Under crosswind conditions, when HSTs move from one infrastructure scenario to another, the aerodynamic loads and pressure field will change rapidly, and the dynamic behaviors of the HSTs become severely deteriorated. Therefore, it is difficult to guarantee train safety and passenger comfort (Liu, 2019). For example, train accidents often occur in the Baili wind area in the LanZhou– Xinjiang Railway line in China (Zhang et al., 2015). In 2007, 11 carriages of a passenger train overturned when the train passed through a section with a wind-break wall at a speed of 36 km/h, causing three deaths and two serious injuries. According to the anemometer records, the instantaneous wind speed at the accident site exceeded 37 m/s. This was due to the sudden increase in the aerodynamic forces when the train left the wind-break wall, which resulted in significant deterioration of the aerodynamic performance. Therefore, investigating the aerodynamic performances of trains traveling from one infrastructure to another is of great significance to ensure the safety of the trains.

Studies on aerodynamic performances of vehicles passing through sections connecting different infrastructures under strong crosswinds are rare. Zhang et al. (2019) studied the aerodynamics of HSTs passing through embankment–cutting connections under crosswinds through wind tunnel tests. Miao et al. (2014) numerically investigated the transient aerodynamics when an HST exited a tunnel with crosswinds at the tunnel exit. Chen et al. (2017) and Zhou et al. (2017) studied the pressure waves in the tunnel for cases of a single-marshalling train passing through and two single-marshalling trains meeting in a double-track tunnel with ambient wind, respectively; however, the aerodynamic performances of the HSTs were not analyzed, and only the situation in which the ambient wind direction was parallel with the direction of the train travel was considered. In fact, when an HST enters or exits a tunnel under crosswinds, the aerodynamic performance will deteriorate significantly, which may result in overturning or derailment. Therefore, studying the aerodynamic performance when a train enters or exits a tunnel under a crosswind is of great significance to ensure the train safety and passenger comfort.

In this study, a numerical model was established that included a crosswind, high-speed train, and tunnel. The aerodynamic performance including aerodynamic load and flow structure when an HST entered the tunnel under a crosswind was then analyzed. The sliding mesh technique and the shear stress transport (SST) k-ω turbulence model were employed in the calculations. Furthermore, qualitative evaluation of the operational stability as the HST entered a tunnel with crosswinds was conducted. The research thus provides a reference for the operation safety of HSTs running in windy mountainous areas.

2. Methodology

2.1. Governing equations

As a HST passes through a tunnel, the air flow is highly unsteady (Niu et al., 2020; Liu et al., 2017; Zhang et al., 2017). Generally, the air is treated as incompressible for cases in which the Mach number ($Ma = v_{tr}/c$, where v_{tr} and c represent the train speed and speed of sound, respectively) is less than 0.3. Although Ma here was less than 0.3, the air in confined spaces such as tunnels is highly compressed while trains pass through. Therefore, the compressibility of air should be considered (Takanobu and Kozo, 1997; Ricco et al., 2007; Li et al., 2019). Thus, a 3-D, compressible Navier–Stokes equation coupled with an unsteady SST $k-\omega$ turbulence model was employed to simulate the process of the HST entering a tunnel under crosswinds.

The SST k-ω turbulence model considers the transport of the turbulent shear stress in the definition of the turbulent viscosity (Menter, 1994). Its range of applications is wider, and the resultant accuracy and reliability are better than the standard k-ω model. Previously, the SST k-ω model was employed to analyze the issues related to the aerodynamics of high-speed railway tunnels (Yao et al., 2020; Liu et al., 2018; Wang et al., 2018; Horvat et al., 2020).

The SST k-ω turbulence model can be expressed as follows:

$$\frac{\partial \rho\kappa}{\partial t} + \frac{\partial}{\partial x_i}\left[\rho u_i \kappa - (\mu + \sigma_\kappa \mu_t)\frac{\partial \kappa}{\partial x_j}\right] = \tau_{tij} S_{ij} - \beta^* \rho\omega\kappa, \tag{1}$$

$$\frac{\partial \rho\omega}{\partial t} + \frac{\partial}{\partial x_i}\left[\rho u_i \omega - (\mu + \sigma_\omega \mu_t)\frac{\partial \omega}{\partial x_j}\right] = P_\omega - \beta\rho\omega^2 + 2(1-F_1)\frac{\rho\sigma_{\omega 2}}{\omega}\frac{\partial\kappa}{\partial x_i}\frac{\partial\omega}{\partial x_j}. \tag{2}$$

where t is time; ρ is the air density; κ and ω are the turbulence kinetic energy and turbulence dissipation ratio, respectively; x_j is the direction coordinate; the subscripts $j = 1$, 2, and 3 represent the x, y, and z directions, respectively; u_j refers to the slipstream components; σ_ω, $\sigma_{\omega 2}$, σ_κ, β, β^*, and γ are empirical constants; F_1 is a switch function; and μ_t is the vortex viscosity coefficient.

2.2. Geometric model and boundary conditions

The standard electric multiple unit (EMU) of CRH380 A in China were employed in this work as the train model, as shown in Fig. 1(a). The train was 3.7 m high and 3.38 m wide. If all the detailed structures, such as bogies, pantographs, and windshield wipers, were considered, the calculational expense would increase significantly. To keep the computational cost low, the prototype train was simplified appropriately, and minor structures such as bogies, pantographs, and the gap between the carriages were omitted. To consider the influence of the structures under the train on the airflow, the distance between the train bottom and the rail top surface was set at 0.2 m (Li et al. 2021). Flow structures appeared in the regions near the train surface when the flow passed a certain distance from the head car nose remained stable due to the unchanged cross-sectional shape in the middle of the train (Cooper, 1981; Khier et al., 2000; Ford and Riskowski, 2003). Therefore, the train employed in this work included three vehicles: one leading vehicle, one middle vehicle, and one rear vehicle. The scale ratio of the train was 1:1, and the length was 77 m, as shown in Fig. 1(b). The train speed was 350 km/h. The Reynolds number Re based on the train height H and the train speed v_{tr} was 2.46×10^7.

The cross-sectional area of tunnel model was 100 m^2, to represent a typical double-track high-speed railway tunnel widely used in China. The centerline distance between the two tracks was 5 m, and the length of tunnel was 500 m, as shown in Fig. 2.

The HST was separated from the tunnel entrance by 145.83 m to ensure the status of the initial flow was steady as the train moved suddenly, which is larger than the values reported in the literature (Liu et al., 2019; Jiang et al., 2019). The computational domain is presented in Fig. 3. The time $t_0 = 1.50$ s corresponded to the instant when the nose tip of the head vehicle reached the tunnel entrance. The moment at which the HST entered completely was about $t = t_0 + L_{tr}/v_{tr} = 2.292$ s, where L_{tr} and v_{tr} represent the train length and train speed, respectively. To ensure the convergence of the aerodynamic forces acting on the train, the calculations was not terminated until the nose tip of the rear vehicle passed the tunnel entrance by 130 m. The computational domains adjoined the tunnel were cuboids. The dimensions of the exterior domains at the tunnel entrance and exit were 350 m × 120 m × 60 m, and 50 m × 50 m × 60 m, respectively. The blockage ratio of the domain at the tunnel entrance was 1.36%, which satisfied the requirements on the blockage ratio defined in BS EN14067-6 (2018).

Two methods, the moving mesh method and the sliding mesh method, were considered to simulate the train movement in the CFD analysis. The former method required a higher mesh quality and computational cost. To improve the calculation efficiency, the sliding mesh technique was adopted. Previous research showed that the sliding mesh method could reflect the relative motion between the train and the surroundings (Miao et al., 2020; He et al., 2018; Chu et al., 2014; Xiang and Xue, 2010; Khayrullina et al., 2015).

The computational domain was divided into a moving zone and a stationary zone. The former contained the train and the surrounding air, as shown in Fig. 4. The latter remained static during the calculations. The flow information between the two zones was exchanged at the interface at each time step.

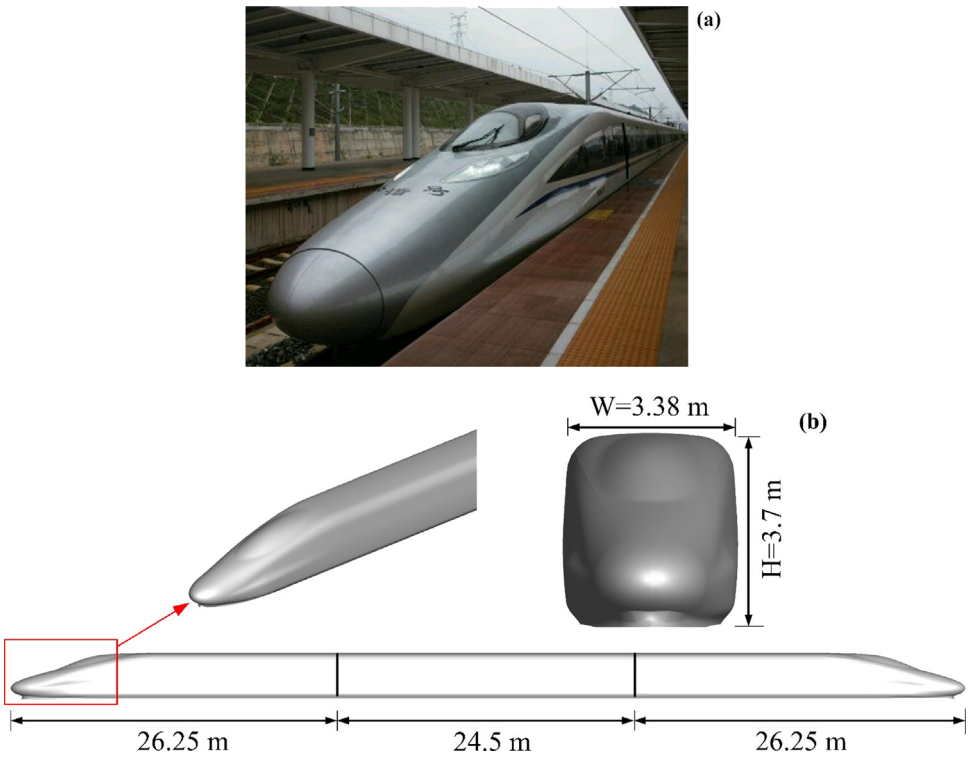

Fig. 1. High-speed train: (a) full-scale train and (b) three-vehicle train.

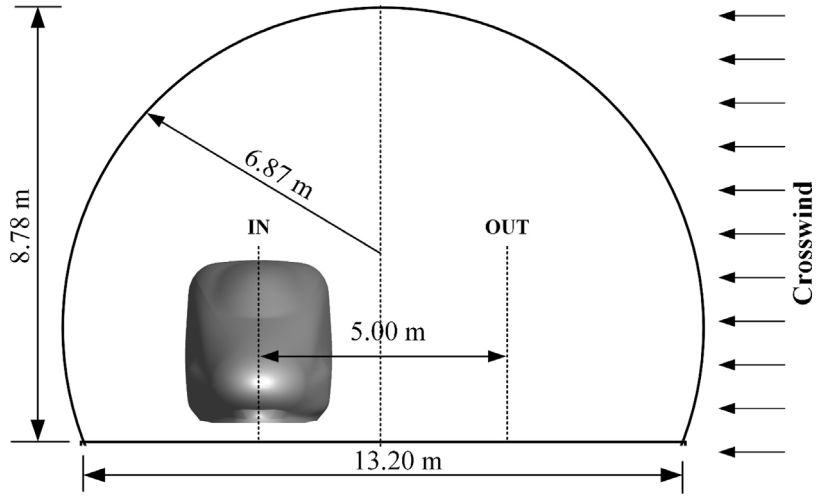

Fig. 2. High-speed railway tunnel.

The boundary conditions are also presented in Fig. 4. A uniform velocity-inlet BC was applied at the crosswind entrance. According to the statistics of the daily wind speed of eight big cities along the high-speed railway from Beijing to Shanghai in China, the wind speed can exceed 30 m/s. Although this wind speed occurs less frequently, it can be devastating to train travel. Therefore, the wind speed was 30 m/s in this study. Non-slip wall BCs were selected at the train surfaces, the tunnel wall, and the ground surface (Hemida and Krajnović, 2010; Wang et al., 2017). Pressure-outlet BCs were applied at the other vertical and top surfaces of the domain, and the total pressure value used was one standard atmosphere. It should be noted that the global coordinate system was shown in Fig. 4, the x-axis represented the direction of train motion, and the y- and z-axes corresponded to the transverse and vertical directions, respectively.

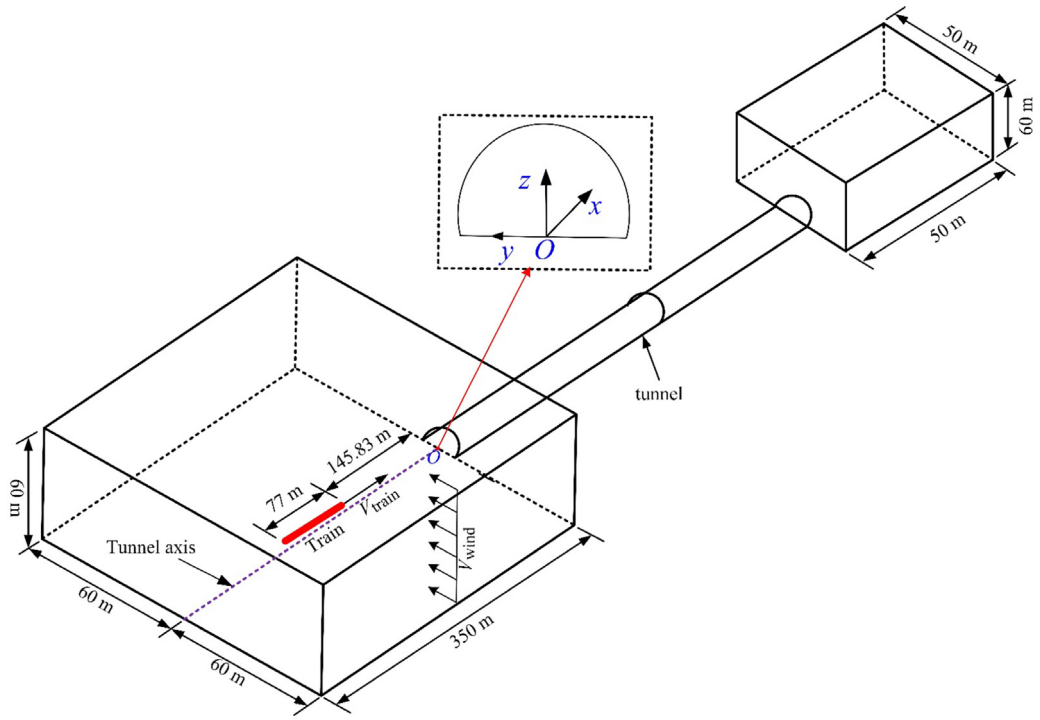

Fig. 3. Diagram of computational domain.

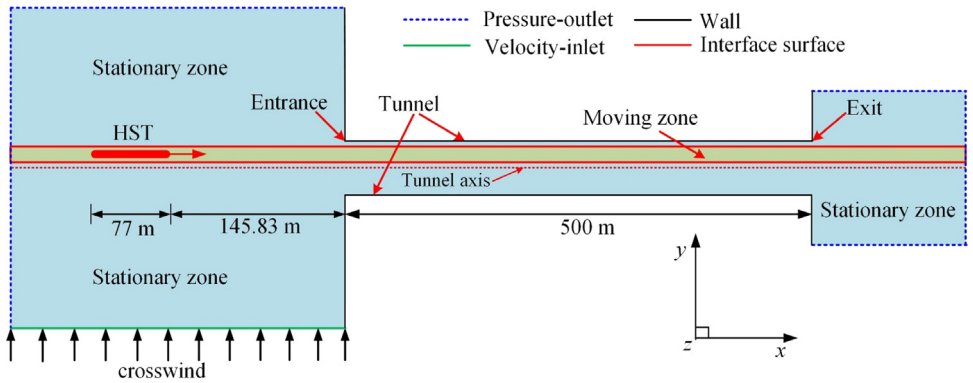

Fig. 4. Diagram of boundary conditions.

2.3. Mesh strategy

The computational domain was discretized with a hexahedral structured mesh. The surface mesh of the tunnel entry and head train are illustrated in Fig. 5. To accurately simulate the flow structures near the train surface, it was necessary to resolve the boundary layer developed on the train exterior surfaces. The height of the 1st grid layer close to the train surface was 0.01 mm, the corresponding $y+$ value was less than 1, and the grid thickness growth ratio was 1.1. Mesh refinement was applied near the head vehicle and the rear vehicle because the cross-sectional shapes of these zones changed rapidly. The minimum mesh size of the train surfaces was 0.01 m. Along the train length, the mesh size in the middle of the train was 0.5 m because the cross-sectional shape of the intermediate vehicles remained nearly unchanged. The mesh size of the tunnel was 0.5 m, and the total number of mesh cells was 10.6 million.

2.4. Solution process

The calculations were carried out using ANSYS Fluent 17.1. The three-dimensional, compressible, unsteady Navier–Stokes equations were solved by the finite volume method. The SIMPLE (semi-implicit pressure linked equations)

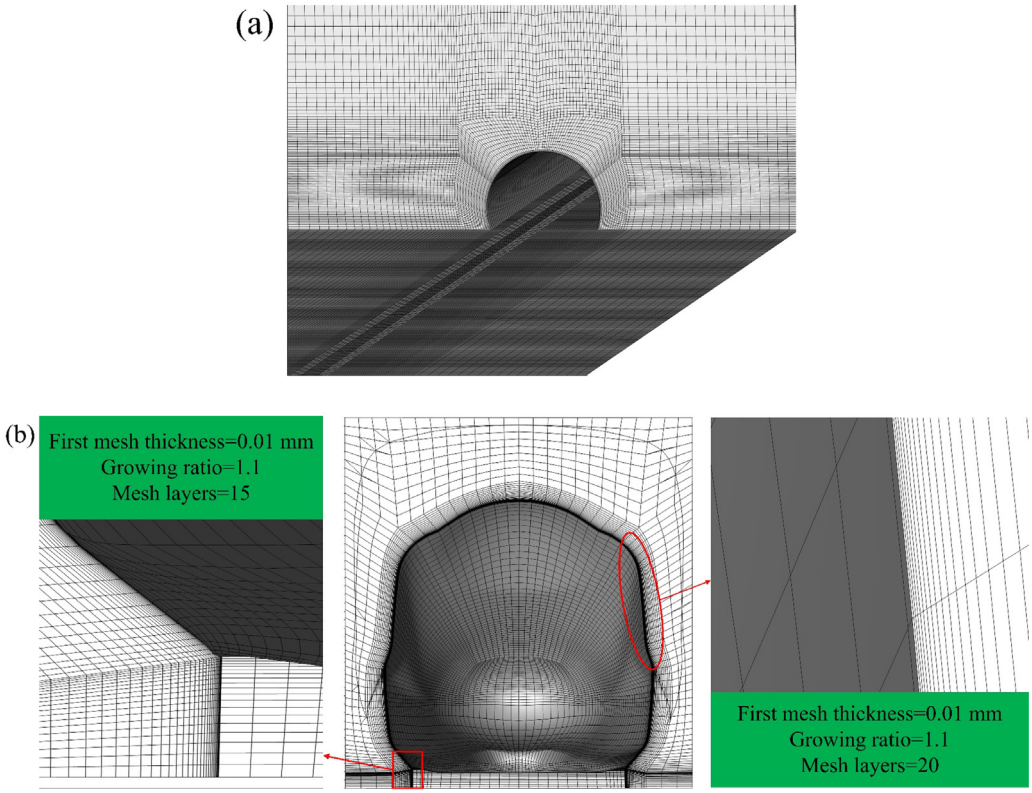

Fig. 5. Mesh on surface in this paper: (a) tunnel entrance and (b) train head surface.

algorithm was implemented for pressure–velocity coupling. The pressure was corrected by an iterative method. The second-order upwind scheme was used for the convection and diffusion terms, and the first-order implicit scheme was used for the time derivative term. The physical time-step was 0.001 s, and the number of iterations for every time step was 20. The CFL number was lower than 1 in 99% of the domain while the CFL number in the regions near the train surface was higher than 1. Therefore, the step time chosen here was considered appropriate. The residuals of the turbulent terms were not allowed to exceed 10^{-3} for each time step (Niu et al., 2017b; Yang et al., 2019). The solution dates were output using a user-defined function (UDF) in Fluent.

2.5. Data analysis

According to the CEN European Standard (2003), a dimensionless index called the pressure coefficient was defined:

$$Cp = (P - P_{\infty}) / 0.5\rho {v_{\mathrm{tr}}}^2. \tag{3}$$

where ρ is the air density (1.225 kg/m^3), P represents the static pressure, P_{∞} is the pressure infinitely far from the train (1 standard atm.), and v_{tr} is the train speed.

In addition to the pressure coefficient, the non-dimensional coefficients, including the side force, lift force, and rolling moment (Suzuki et al., 2003; Miao and Gao, 2015), were defined, which affected the aerodynamic behaviors of the trains most significantly:

$$C_s = F_s / 0.5\rho {v_w}^2 A, \tag{4}$$

$$C_l = F_l / 0.5\rho {v_w}^2 A, \tag{5}$$

$$C_m = M / 0.5\rho {v_w}^2 A h. \tag{6}$$

where C_s, C_l, and C_m denote the side force coefficient, lift force coefficient, and rolling moment coefficient, respectively; F_s, F_l, and M denote the side force, lift force, and rolling moment, respectively; A refers to the area to the windward surface of the HST; and h is the train height.

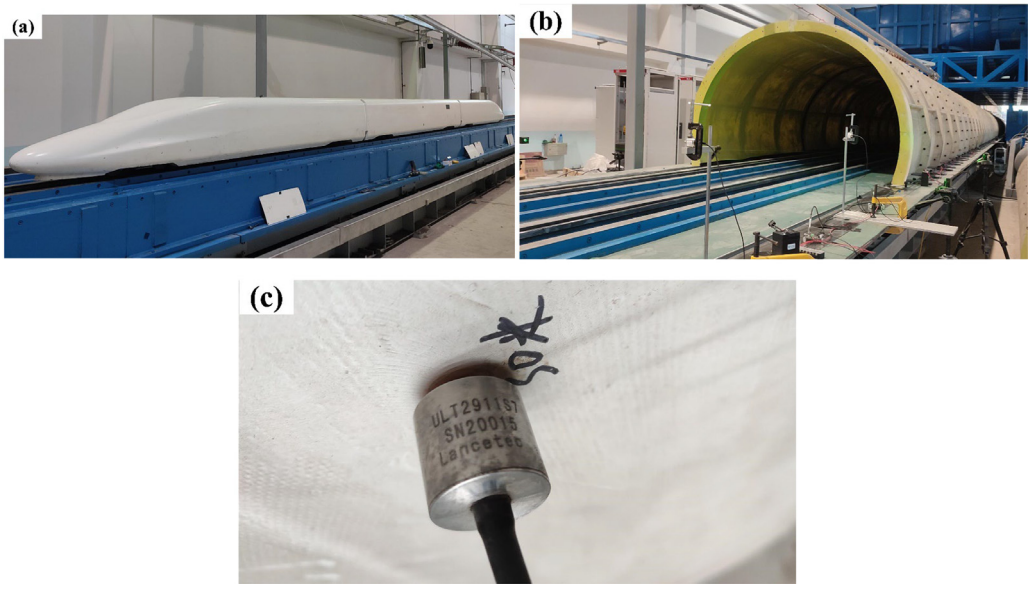

Fig. 6. Moving model rig: (a) HST, (b) double-track tunnel, and (c) pressure sensor.

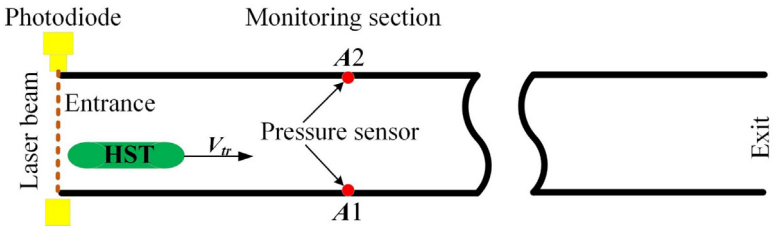

Fig. 7. Position diagram of pressure sensors.

3. Validation

We selected moving model test results to validate the accuracy of the numerical algorithm. The moving model test was performed at the Advance Railway Mechanics Center (ARMC), Institute of Mechanics, Chinese Academy of Sciences at Huairou District, Beijing. The detailed information about the experimental facilities was provided by Yang et al. (2013, 2016). The scale ratio of the model was 1:8, and the train model included three vehicles, which was 9.9 m long, as shown in Fig. 6(a). The train speed was 304 km/h (84.44 m/s). The tunnel was 60 m long, and it was a double-track railway tunnel commonly used in China, as shown in Fig. 6(b). Model ULT2911S7 static pressure sensors produced by Quatronix Products Inc. were used in this test, as shown in Fig. 6(c). The measurement range of the sensor was up to ±7 kPa, its sample frequency was 5 kHz, and its sensitivity was 2.86 mV/100 kPa. The sensors were calibrated, and the measurement error was less than 1% before the test. The sensors were installed on the tunnel wall 20 m from the tunnel entrance and 471 mm above the tunnel bottom surface, as shown in Fig. 7. To reduce the influence of the Reynolds number on the test results, the scale ratio of the model in the simulations was consistent with the moving model test.

Fig. 8 shows the comparisons of the static pressures between the simulation and experiment of pressure sensors A1 and A2. The numerical and experimental results as the train traveled through the tunnel showed reasonable agreement. The main indexes to estimate the pressure difference between experimental and numerical results are the positive peak pressure (P_{maximum}), negative peak pressure (P_{minimum}), and peak–peak pressure, as shown in Table 1, whose deviations of pressure sensor A1 are observed to be 3.1%, 3.7%, and 1.1%; the deviations of pressure sensor A2 are observed to be 2.4%, 2.3% and 0.4%, respectively. Thus, the calculation accuracy could meet the engineering requirements.

Fig. 9(a) shows the flow distribution of the CRH380 A high-speed EMU, with a head vehicle and a rear vehicle, when the train traveled on level ground at 350 km/h (97.22 m/s) under a crosswind (30 m/s). Fig. 9(b) shows the flow structures on the leeward side surface of the head vehicle under crosswinds reported by Copley (1987). Vortex sheets were formed on the train's leeward side due to the flow separation, and several vortices appeared along the train length. Therefore, it was concluded that the numerical algorithm was valid and the results was reliable. However, it is noteworthy that vortex

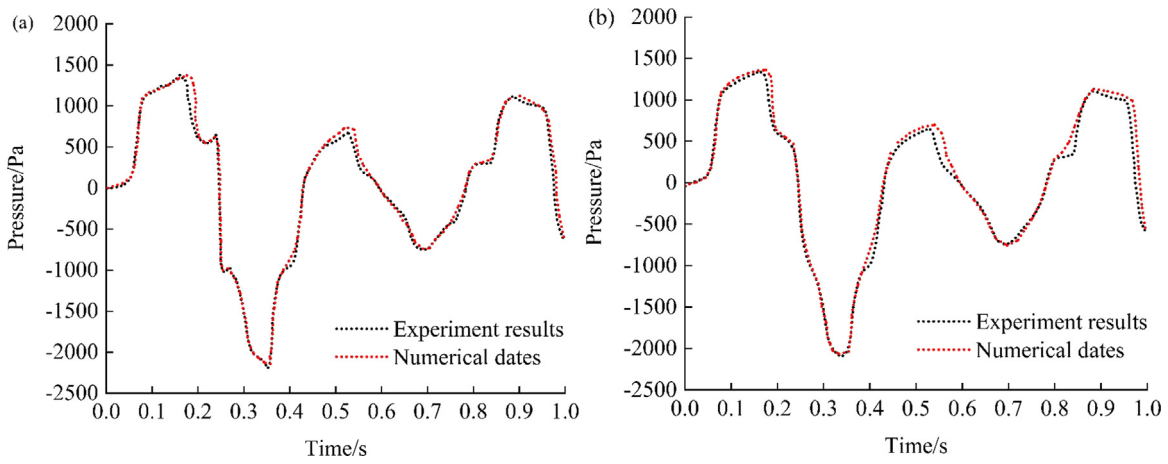

Fig. 8. Comparison of the numerical and experimental test results: (a) Pressure sensor A1; (b) Pressure sensor A2.

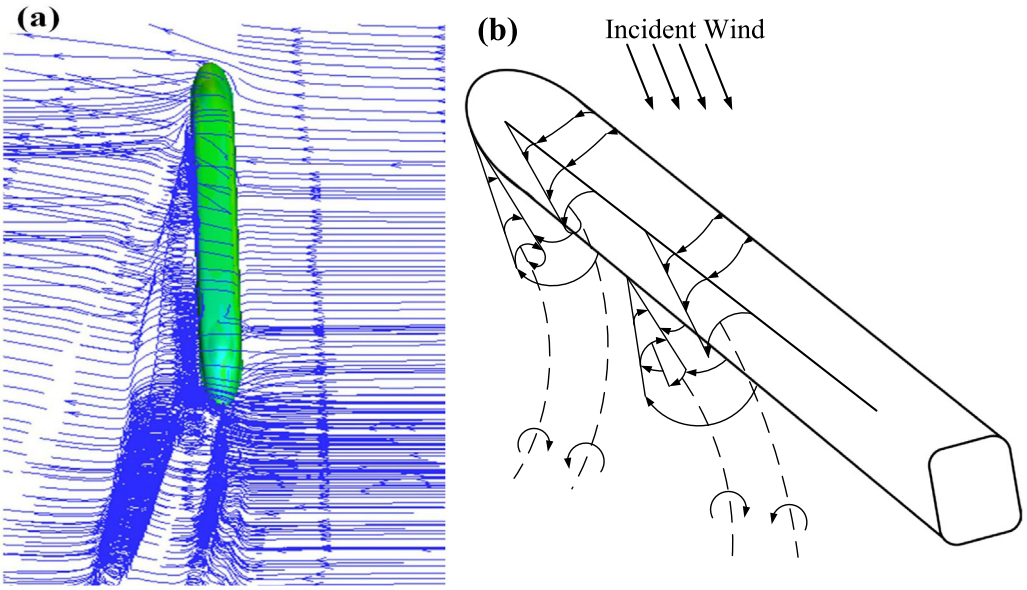

Fig. 9. Comparison of flow field: (a) numerical results; (b) experimental results of Copley (1987).

Table 1
Main indexes for estimating pressure change.

Pressure sensor ID	variable	Moving model test results (Pa)	Numerical results (Pa)	Deviation (%)
A1	$P_{maximum}$	1347	1389	3.1
	$P_{minimum}$	−2221	−2141	3.7
	peak-peak pressure	3568	3530	1.1
A2	$P_{maximum}$	1340	1372	2.4
	$P_{minimum}$	−2111	−2064	2.3
	peak-peak pressure	3451	3436	0.4

shedding from the tail carriage was evident in Fig. 9(a), while it was not evident in Fig. 9(b). This was because there was some difference in the shapes of the tail carriages and the train speed.

4. Results and discussion

4.1. Flow structure

When a high-speed train passes through a tunnel, a strong slipstream is generated between the train and the tunnel walls due to the piston effect, which results in a transient change of the flow field. Fig. 10 shows the development process of the flow field when the train entered the tunnel on the horizontal plane located at $z = 1.05$ m (the height of the nose tip of the train). The Figs. (a1)–(e1) correspond to the case with no crosswind, and the Figs. (a2)–(e2) correspond to the case with a crosswind of 30 m/s. For convenience, the windward and leeward side surfaces of the train are henceforth referred to as the WS and LS, respectively.

When the nose tip of the train entered the tunnel, the flow field was symmetrically distributed about the train axis with no crosswind, and the air flowed from the nose tip of the head vehicle to the tail, as shown in Fig. 10(a1). When the train entered the tunnel with a crosswind, a vertical vortex (shown as Vortex A in Fig. 10(a2)) appeared in the tunnel near the entrance, which was induced by the combined interactions of the slipstream and the crosswind. However, a longitudinal vortex (shown as Vortex B in Fig. 10(a2)) was generated on train's LS, which started from the leeward surface of the streamlined section of the head vehicle and deviated from the train along the length of the train.

The air ahead of the train flowed towards the tunnel exit along the direction of the train motion, and the air in the annular space between the tunnel and the train flowed towards the entrance of the tunnel as the train entered with no crosswind. In addition, the flow field was distributed symmetrically about the center of the track.

When a crosswind was present at the tunnel entrance, the air ahead of the train flowed towards the exit of the tunnel, and the air between the tunnel and the train flowed backwards in the direction of the tunnel entrance. However, when the airflow on the WS reached the tunnel entrance, its flow direction changed suddenly and flowed back into the tunnel again due to the crosswind. The influence of the crosswind on the airflow ahead of the train decreased gradually as the train passed through the tunnel. The position of Vortex A shifted from the front of the train to the WS of the train, as shown in Fig. 10(b2).

As the axial center of the head vehicle entered the tunnel, the length of Vortex A increased gradually. Due to the shielding effect of the tunnel, the vortex located on the LS of the carriages inside the tunnel disappeared, while Vortex B situated on the LS of the carriages outside the tunnel was still present, and its initial position was at the entrance of the tunnel, as shown in Fig. 10(c2). The flow field distribution as the center of the rear vehicle entered the tunnel is presented in Fig. 10(d2). Vortex A located on the WS of the train decomposed into several small vortices because the influence of the ambient wind on the airflow in front of the train decreased steadily, and the energy of the flow attenuated as it flowed out of the tunnel. In addition, it is also noteworthy that two longitudinal Vortices B and C were present on the LS of the train, and the axes of the vortices were distributed parallelly. As the nose tip of the rear vehicle entered the tunnel, as shown in Fig. 10(e2), Vortex C disappeared, while Vortex B existed until the train entered the tunnel completely.

Fig. 11 shows the surface streamlines when the center of the HST entered the tunnel when crosswind conditions existed and when they did not. Figs. 11(a1) and (a2) show that the streamlines of the surfaces of the train were distributed symmetrically with respect to the train centerline, and a pair of wake vortices existed behind the rear vehicle when the train entered when there was no crosswind.

In contrast, the streamline distributions on the train surfaces were significantly asymmetric as the train entered with a strong crosswind. The streamlines on the train surfaces outside the tunnel flowed from the WS to the LS, and flow separation occurred at the upper and lower edges of the LS, as shown in Figs. 11(b2) and (d2). In addition, it was concluded from Fig. 11(c2) that a significant flow separation phenomenon occurred on the LS of the streamlined section of the rear vehicle. However, the streamlines of the surfaces of the WS and LS inside the tunnel were almost the same, and the symmetry of the top and bottom surfaces of the train was poor, because these areas were affected significantly by the crosswind.

4.2. Pressure distribution on train surface

Fig. 12 presents the pressure distributions at the same instances of plots shown in Fig. 10. The pressure of the surface near the nose tip of the head and rear vehicle were positive, and the largest positive pressure was positioned at the nose tip of the head vehicle as the head vehicle entered the tunnel with no crosswinds, as shown in Fig. 12(a1). Like the flow field, the pressure distributions on the WS and LS were the same, and the pressure was distributed symmetrically about the train centerline. The pressure on WS of the rear vehicle was negative, while the pressure on the remaining areas of the WS were positive as the nose tip of the head vehicle reached the entrance with crosswinds, as shown in Fig. 12(a2). The pressures on LS were negative, and the position of the maximum positive pressure moved from nose tip of the head vehicle with no crosswinds to the WS under crosswinds. Therefore, a strong side force was generated because a large pressure difference existed on the WS and LS. The lateral displacement appeared on the LS of the train. It was concluded from Figs. 12(a1) and (a2) that the pressure field was distributed symmetrically under non-crosswind conditions, while the pressure field shifted to the LS of the train under crosswind conditions.

When the train entered the tunnel with no crosswind, as shown in Figs. 12(b1)–(e1), the surface pressure of the train inside the tunnel was positive, and the pressure distributions on the WS and LS were basically the same. Although the

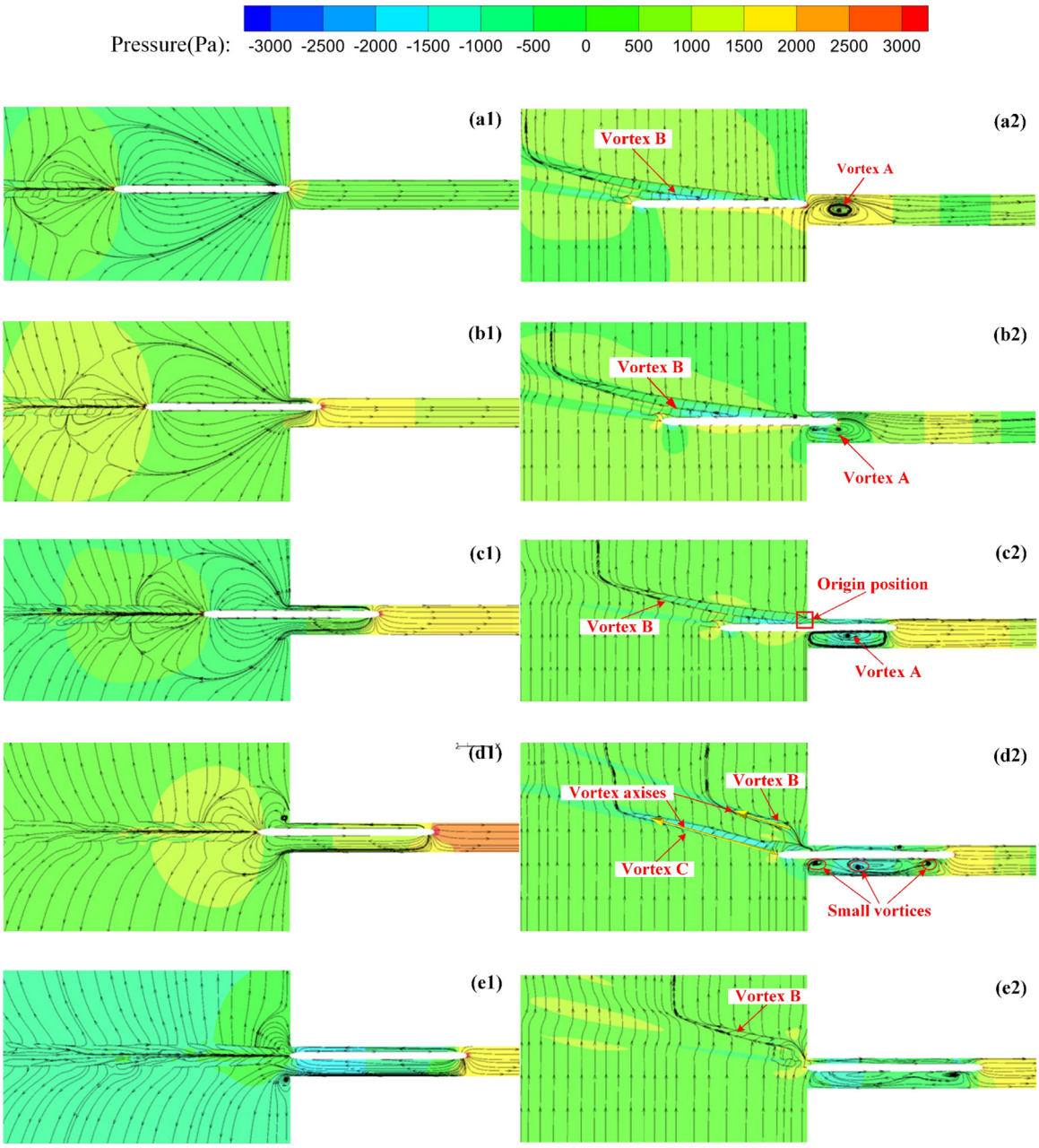

Fig. 10. Comparison of the flow field when train is entering the tunnel. The Figs. 10(a1)–(e1) correspond to the case with no crosswind, and Figs. 10(a2)–(e2) correspond to the case with a crosswind of 30 m/s.

traveling direction of the train did not coincide with the centerline of the tunnel, it had little effect on the pressure distribution. Overall, the pressure field around the train was still distributed symmetrically.

When the train entered the tunnel with crosswinds, the pressure of the train surface changed gradually. Affected by the shielding effect of the tunnel, the area of the WS decreased gradually, and the pressure of the WS inside the tunnel changed rapidly from positive to negative, and the pressure distributions on the WS and LS were basically the same. Nevertheless, the pressure distribution on WS outside the tunnel remained unchanged, and the aerodynamic side force was significant. Therefore, the aerodynamic loads acting on the same carriage inside and outside the tunnel showed significant differences, which would have significant adverse effects on the structures and the safe operation of the train, as presented in Figs. 12(b2)–(d2). As the train entered completely, the pressure distributions on the WS and LS were similar, and the influence of the crosswinds on the stability of the train disappeared slowly, as shown in Fig. 12(e2).

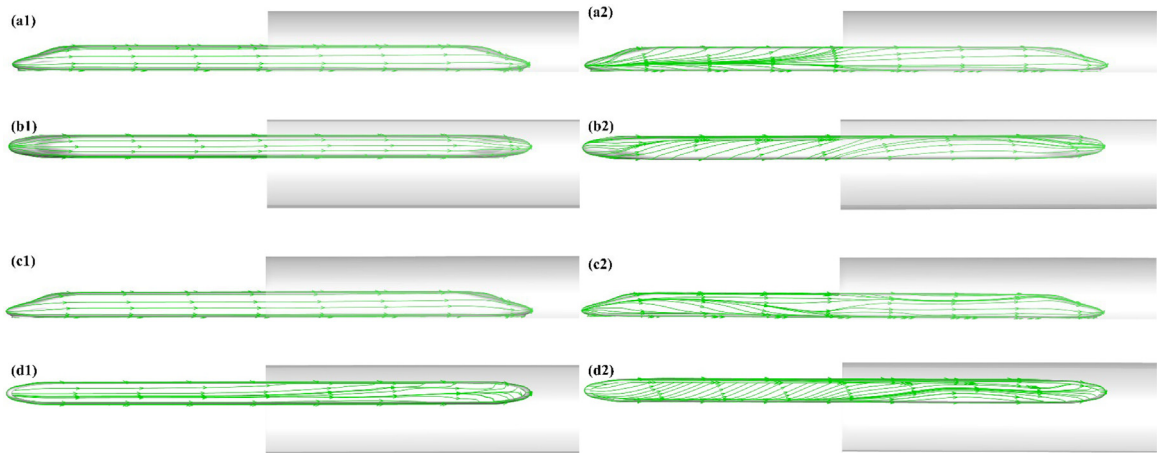

Fig. 11. Surface streamlines on (a) windward side surface, (b) top surface, (c) leeward side surface, and (d) bottom surface when the middle of the HST entered the tunnel. The plots on the left and the right columns represent non-crosswind and crosswind conditions (30 m/s), respectively.

Fig. 13 shows the two-dimensional streamlines and pressure distributions on cross sections at different positions, and Fig. 13(a) shows the positions of the cross sections. Figs. 13(b)–(d) correspond to the flow field distributions and the pressure coefficient curves of the train surface when the center of the head vehicle, the center of the train, and the center of the rear vehicle entered the tunnel, respectively. As the middle of the head vehicle entered the tunnel, the surface pressure on S1 and S2 inside the tunnel were all negative, and the maximum pressure appeared on the top of the train. Vortex V1 appeared at the bottom of the tunnel on the LS due to the blocking effect of the tunnel; therefore, V1 only existed in the tunnel. When the crosswind flowed to the WS outside the tunnel, the air speed decreased, and the positive pressure increased. The stagnation point appeared on the WS, where the positive pressure was the largest. The crosswind flowed downstream along the train surface, and the maximum negative pressure appeared at the upper corner of the WS, as shown at point A in Fig. 13(b). The magnitudes of the negative pressure outside tunnel were much larger than those inside the tunnel. In addition, flow separation occurred at the top and the bottom of the LS, forming two shedding vortices, V2 and V3. Fig. 13(b) shows that V2 was formed earlier than V3.

When the center of the train arrived at the tunnel entrance, the flow field of S6 inside the tunnel was similar to that of S2, as shown in Fig. 13(b), and the differences along the train surface were mainly concentrated at the bottom, since S2 was located in the streamlined section and the flow at the bottom was unstable. A comparison of S6 with S7 shows that vortices V2 and V3 located on the LS inside the tunnel disappeared gradually after the train entered the tunnel. The flow field distributions of S8 and S9 outside the tunnel were similar, and pressure differences occurred on the LS, as shown in Fig. 13(c). Hemida and Krajnović (2009) explored flow structures around the HST subjected to a 30° side wind. They found that higher values of C_s were associated with the smallest distance between the centers of the vortices and the LS surface of the train because of the lower pressure on the LS surface. The distances from the vortex core of V3 to the ground were 0.86 and 1.22 m, and the horizontal distances to LS were 1.14 and 0.95 m, respectively. Therefore, the LS in S9 was even more affected by V3, and the negative pressure was higher than that in S8.

When the center of the rear vehicle entered the tunnel, the flow field and the pressure on the train surface inside tunnel were similar, and the height of V1 increased, as shown in S10 and S11 in Fig. 13(d). S12 and S13 were all located in the streamlined section of the rear vehicle. Aside from the positive pressure on WS in S12, the pressures on the other surfaces were all negative. S13 was located close to the nose tip of the rear vehicle, and the pressures of the train surfaces were all negative. The maximum negative pressure appeared on the WS, as shown at point B in Fig. 13(d).

4.3. Aerodynamic load

When the train entered the tunnel under a crosswind environment, the aerodynamic loads changed rapidly, which resulted in the deterioration of the aerodynamic performances of the train. The risk of train derailment or overturning was high. Fig. 14 shows the time–history curves of the aerodynamic coefficients when the train entered the tunnel. The Figs. 14(a1)–(c1) correspond to the case with no crosswind, and Figs. 14(a2)–(c2) correspond to the case with a crosswind of 30 m/s. The initial distance between the nose tip of the head vehicle and the tunnel entry was 97.22 m.

The values of C_s for each carriage were close to zero because the pressure field was distributed symmetrically, as described in Section 4.2 when the train entered the tunnel with no crosswinds, as shown in Fig. 14(a1). When the head vehicle entered the tunnel, the values of C_s first decreased suddenly and then increased slightly to a stable value (−0.12), with a variation amplitude of 0.13. This showed that the head vehicle was always acted on by the side force toward the WS, and thus, it moved to the WS as it entered the tunnel. The values of C_s for the middle vehicle always remained near

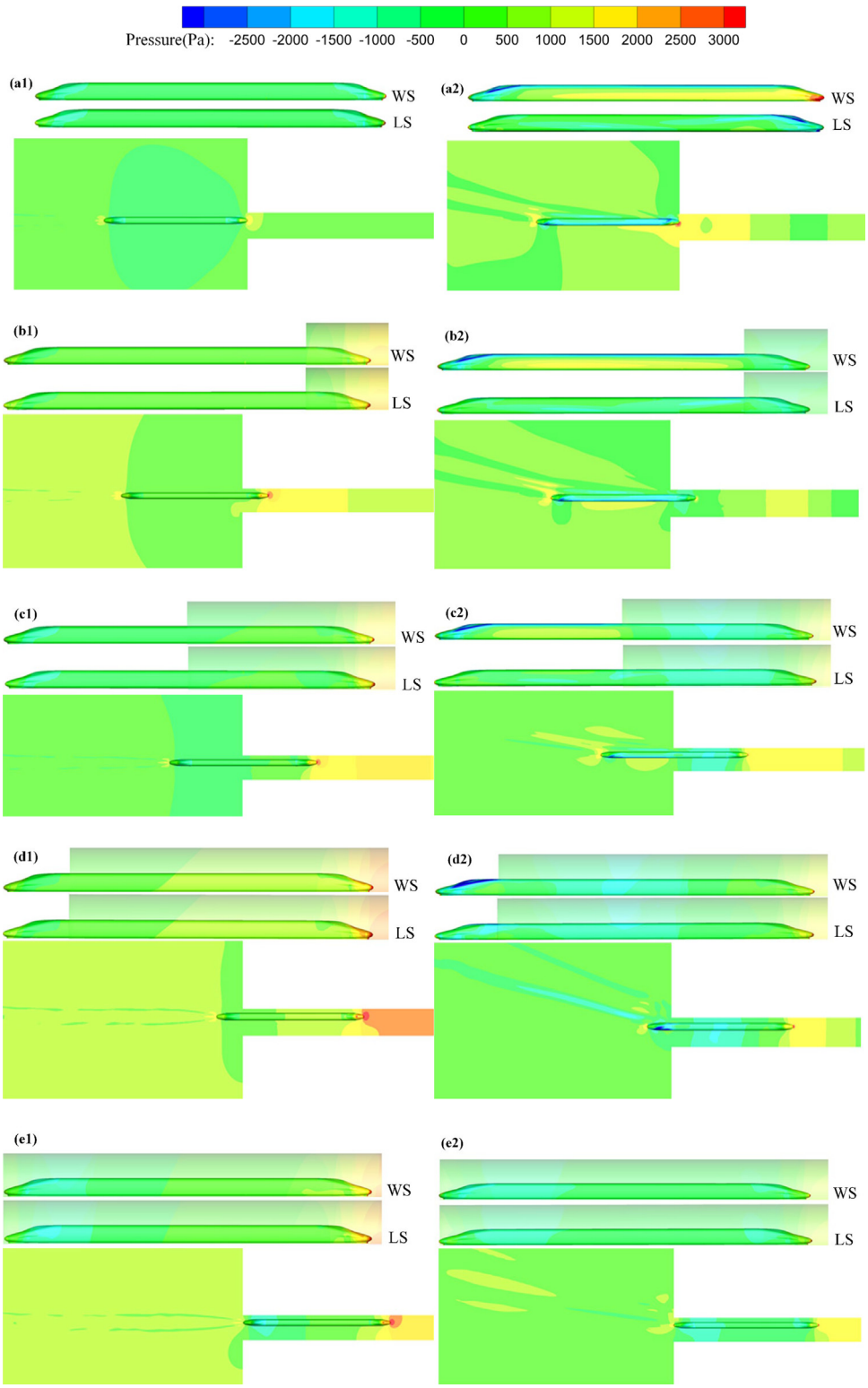

Fig. 12. Comparison of the pressure fields when the train is entering the tunnel. The Figs. 12(a1)–(e1) correspond to the case with no crosswind, and Figs. 12(a2)–(e2) correspond to the case with a crosswind of 30 m/s.

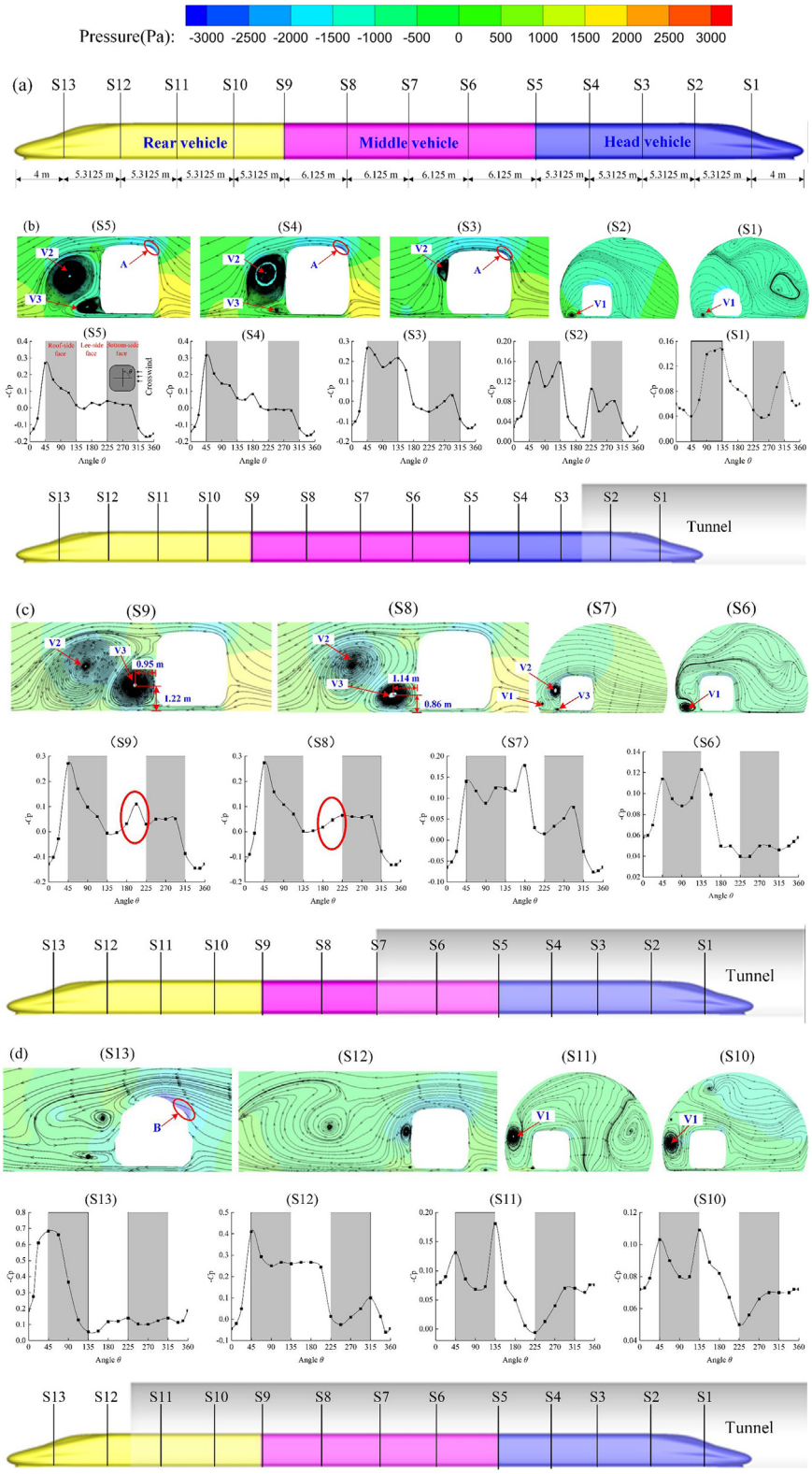

Fig. 13. Streamlines and *C*p values for different positions as the HST entered a tunnel under a crosswind.

zero, which was accompanied by small changes as the middle carriage entered the tunnel. The values of C_s for the rear vehicle fluctuated violently when it entered the tunnel. The maximum and minimum values of C_s for the rear vehicle were 0.288 and −0.266, respectively, and the variation amplitude was 0.554. Therefore, the amplitude and the variation rate of C_s for the rear vehicle were the largest when the train entered the tunnel under non-crosswind conditions.

Before the train entered the tunnel with a uniform crosswind at the tunnel entrance, as shown in Fig. 14(a2), the value of C_s for the head vehicle was the largest (4.66), followed by that of the center vehicle (1.15), and that of the rear vehicle was the smallest (−0.56). When the head vehicle entered the tunnel, the values of C_s decreased sharply, and then it increased rapidly to a stable value (−0.13) with a variation amplitude of 5.56. This indicated that when the train was running in the open air, the side force was directed to the LS. During the process of entering the tunnel, the side force acting on the head vehicle decreased sharply, and it was directed toward the WS. Therefore, when a train enters a tunnel under a strong crosswind, the aerodynamic side force acting on the head vehicle will change suddenly, and it is very likely to derail near the tunnel entrance.

Similar to the head vehicle, the train body deflected to the LS before the middle vehicle entered the tunnel. During the process of the middle vehicle entering the tunnel, the values of C_s decreased monotonically to zero, and the variation amplitude was 1.15. This showed that the side force of the middle vehicle was reduced quickly after entering the tunnel, and the middle carriage kept running steadily. Before the rear vehicle entered the tunnel, the value of C_s was −0.56, and the train was deflected to the WS. The values of C_s for the rear vehicle increased gradually and tended to stabilize at around −0.2, with a variation amplitude of 0.36. This showed that the lateral deviation to the WS was reduced as the train entered the tunnel. A comparative analysis with the head vehicle showed that as the train entered the tunnel, the values of C_s for the head vehicle changed smoothly, while that of the rear vehicle changed more significantly, indicating that the rear vehicle would swing back and forth regularly. In addition, the change ratio of the head vehicle was the largest. The amplitude and the change ratio of C_s for the head vehicle were the largest when the train entered the tunnel with crosswinds, and a derailment accident was the most likely to occur at the tunnel entry. The variation of C_m was the same as that of the side force, because the calculation of the overturning moment was based on the geometric center of each carriage. The amplitude and the change rate of C_m for the head vehicle were also the largest.

When the train ran in the open air with no crosswinds, as shown in Fig. 14(b1), the value of C_l for the head vehicle was negative (−1.36), and the direction was vertically downward. Before the middle train entered the tunnel, the magnitude of C_l was maintained at about 0.07, and the direction was vertically upward, while the values of C_l did not change significantly as it entered the tunnel. The magnitude of C_l for the rear vehicle remained at zero before it entered the tunnel. As the rear vehicle entered the tunnel, the values of C_l fluctuated significantly: it first increased, then decreased, and then stabilized. The maximum and the minimum values of C_l were 0.26, and −0.21, respectively, and the variation amplitude was 0.47. This indicated that the rear vehicle experienced a head-up and head-down movement process as it entered the tunnel. In summary, when the train entered the tunnel under non-crosswind conditions, the amplitude and the change rate of the side force and the lift force were the most significant, and the aerodynamic performance of the rear vehicle was the worst.

When the train ran in the open air under strong crosswinds, as shown in Fig. 14(b2), the values of C_l for each carriage remained stable. The lift force coefficient of the head vehicle was the largest, and its direction was vertically downward, followed by the lift force coefficients of middle vehicle and the rear vehicle. The directions of the lift of the middle vehicle and the rear vehicle were vertically upward. As the head vehicle entered the tunnel, the lift force coefficient fluctuated drastically: it increased suddenly and then decreased sharply, with a magnitude of 0.96, which indicated that the head vehicle underwent a head-up and head-down process. The lift force coefficient of the head vehicle returned to the state running in the open air when it entered the tunnel completely. As the middle and rear vehicles entered the tunnel, the lift coefficient decreased monotonically. After the train completely entered the tunnel, the stable lift force coefficients of the middle and rear vehicles were 0.07 and −0.02, respectively. This indicated that the directions of the lift of the head vehicle and the rear vehicle were vertically downward, while the lift of the middle vehicle was vertically upward. In summary, the side force and lift of the head vehicle changed most significantly, and they were much larger than those of the middle and rear vehicles when the train entered the tunnel under crosswind conditions. The aerodynamic performance of the head vehicle was the worst, and the head vehicle was the most likely to overturn or derail.

In summary, the crosswinds at the tunnel entry had strong impacts on the aerodynamic performance of the train. When the train entered the tunnel with no crosswinds, the aerodynamic performance of the rear vehicle was the worst, and the risk of overturning or derailment was the greatest. In contrast, when the train entered the tunnel from a strong crosswind environment, the side force and the variation rate of the lift force of the heading vehicle were the largest. In addition, the lateral and vertical movements of the head vehicle were the most dramatic, and the risk of accidents was the highest.

4.4. Impact of crosswind direction on aerodynamic load

To investigate the influence of the direction of the crosswinds on the aerodynamic performance of the train, the velocity-inlet boundary condition was applied on the opposite vertical surface of the velocity-inlet boundary surface, as shown in Figs. 3 and 4. To correspond with the previous analysis, the crosswind was perpendicular to the direction of the train movement, and the wind speed was also 30 m/s. For convenience of description, the crosswind in the preceding text is called the upstream-crosswind (UC), while the crosswind here is called the downward-crosswind (DC).

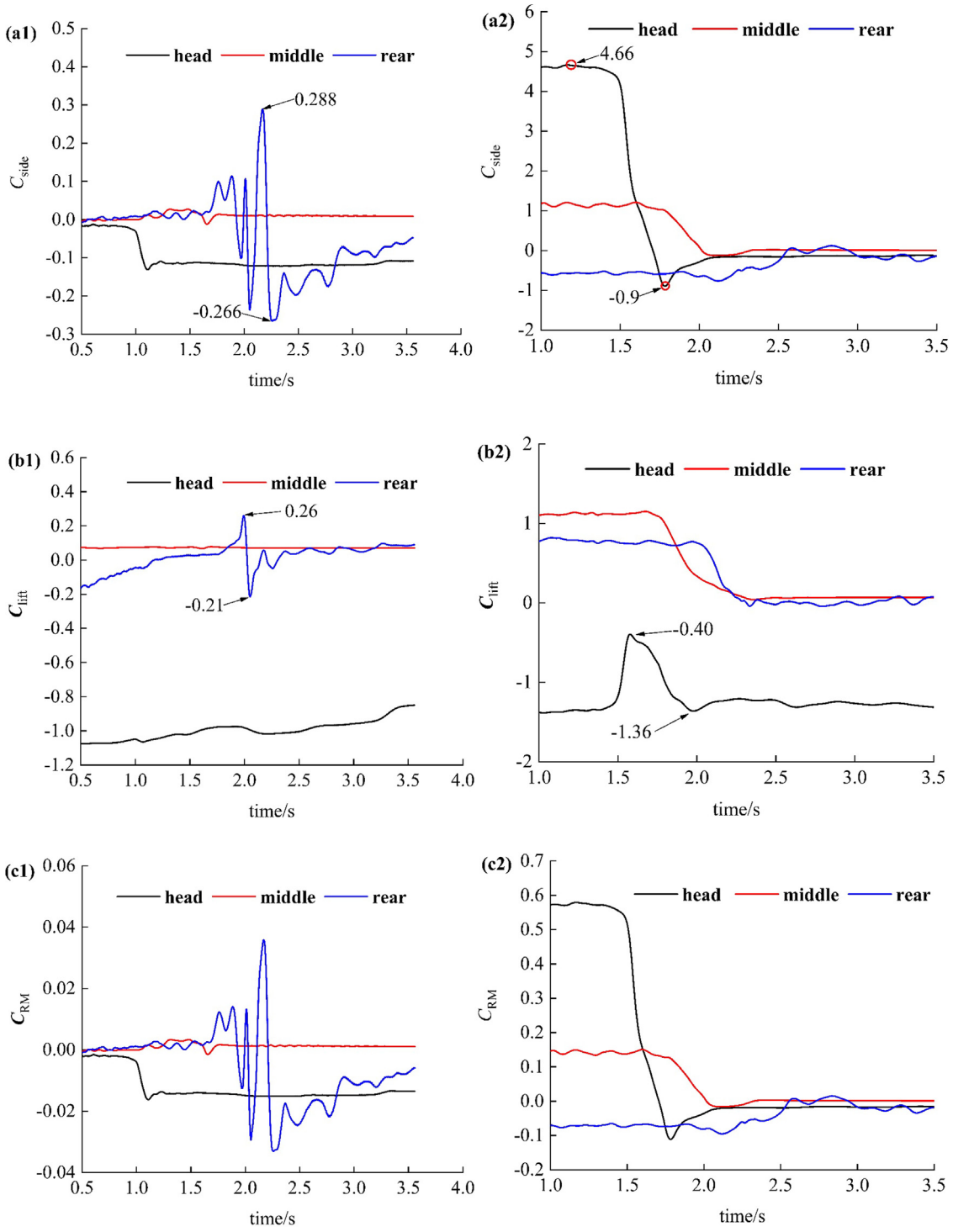

Fig. 14. Evolution of the aerodynamic loads when the HST entered a tunnel. The Figs. 14(a1)–(e1) correspond to the case with no crosswind, and Figs. 14(a2)–(e2) correspond to the case with a crosswind of 30 m/s.

As shown in Figs. 14(a2) and 15(a), little difference in the side force coefficients of each carriage was evident as the train traveled in the open air. When the directions of the crosswinds were different, the variance in the side force was mainly focused on the head vehicle and the rear vehicle. In particular, the magnitude of C_s for the head vehicle decreased quickly and monotonically to a stable value (0.15) under DC conditions, with a variation amplitude of 4.49. The values

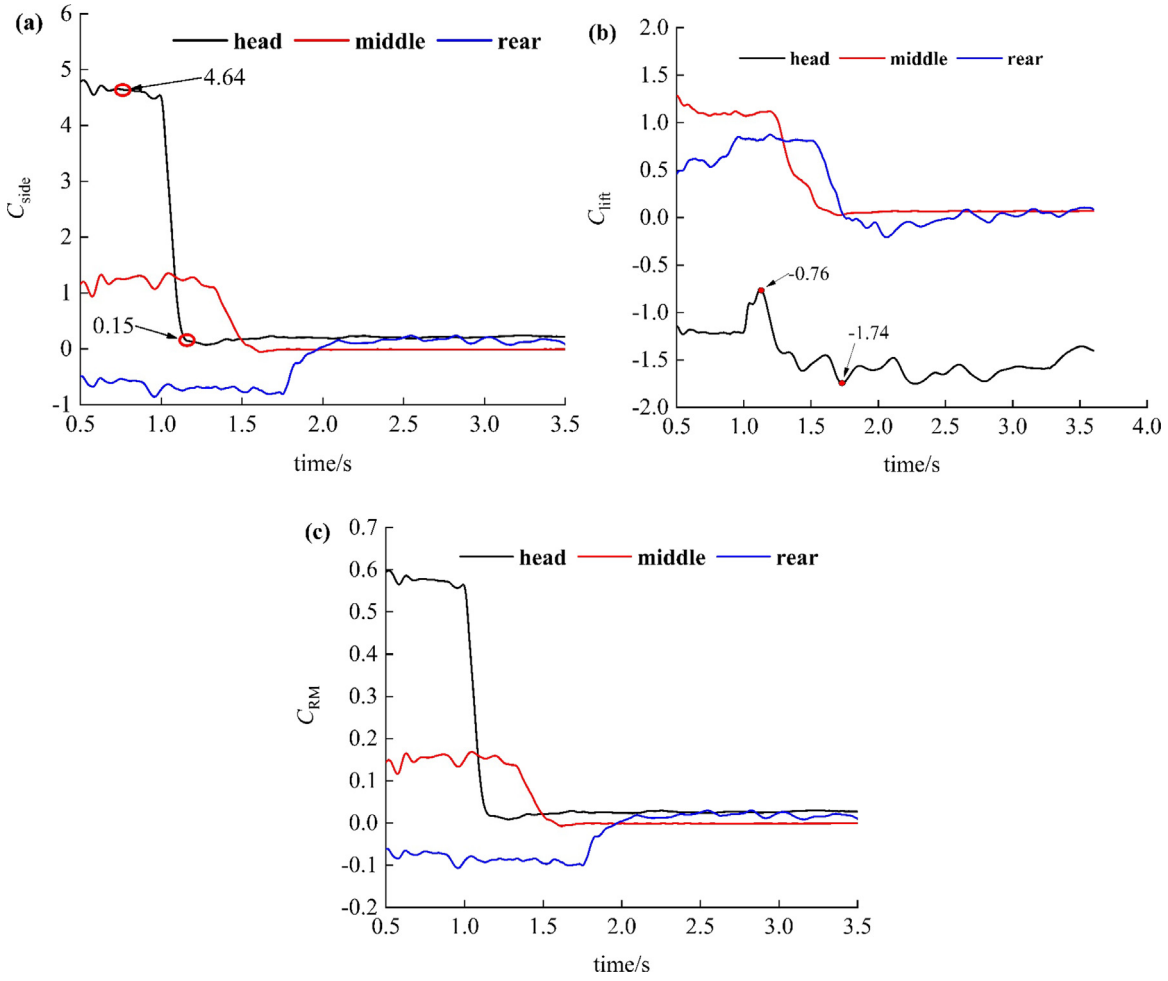

Fig. 15. Evolution of the aerodynamic loads when the HST entered a tunnel with crosswind applied on the opposite vertical surface of the velocity-inlet surface shown in Fig. 3.

of C_s for the rear vehicle increased rapidly and became stable gradually as it entered the tunnel. The directions of the lateral deviation of the head vehicle and the rear vehicle when running in the tunnel were not affected by the crosswind direction. In the two cases with different crosswind directions, the difference between the side force coefficient of the middle vehicle was not significant, indicating that the directions of the crosswind had no impact on the side force of the middle vehicle. The variations of the overturning moment coefficients of each carriage were the same as those of the side force coefficient, as shown in Figs. 14(c2) and 15(c).

The values of C_l for each carriage were almost the same before the train entered the tunnel, as shown in Figs. 14(b2) and 15(b). The diversity of the lift force coefficient was focused on the head vehicle under different crosswinds. When the train entered the tunnel under DC conditions, the lift force coefficient fluctuated significantly, with a magnitude variation of 0.98, which was not much different from the UC conditions. Similar to the side force of the middle vehicle, the directions of the crosswind had no evident influence on the lift force coefficients of the middle and rear vehicles.

Based on the previous comparative analysis, the direction of the crosswinds had no effect on the aerodynamic performance of the train as it traveled in the open air. As the train entered the tunnel, the directions of the crosswind mainly affected the side forces of the head vehicle and the rear vehicle and the lift force of the head vehicle. Furthermore, regardless of the crosswind direction, DC or UC, the aerodynamic performance of the head vehicle was the worst, and its risk of overturning and derailment was the highest.

5. Conclusion

In this work, a three-dimensional, compressible, and unsteady RANS method was adopted to investigate the aerodynamic loads and the flow structures when a high-speed train entered a tunnel with crosswinds. The turbulent flow

structures around the train were calculated by the SST k-ω turbulence model. The sliding mesh method was utilized to model the relative movement between the train and the tunnel. The numerical model was validated by comparison with previous simulations and moving model tests. Some conclusions were as follows:

Firstly, the flow and pressure fields were symmetrically distributed about the train centerline as the train entered the tunnel with no crosswinds. In contrast, the distribution of the flow field and the pressure field showed significant asymmetry when the train entered the tunnel under crosswind conditions. In particular, the flow and pressure fields of the train outside the tunnel were the most severely affected by the crosswinds.

Secondly, under the shielding effect of the tunnel, the pressure on the train surfaces and the flow field as the train arrived at the tunnel entrance varied rapidly when crosswinds were present at the tunnel entrance. As the train continued to enter the tunnel, the influence of the crosswinds on the flow field and the pressure on the train surface decreased gradually.

Thirdly, due to the sudden change in the flow field and the pressure on the train surface, the aerodynamic loads acting on the train changed rapidly, and the variations of the aerodynamic loads of each vehicle were different when the train entered the tunnel. In particular, the aerodynamic performance of the rear vehicle was the worst as the train entered with no crosswinds, while the head vehicle was the most adverse to safe operation when strong crosswinds existed at the tunnel entrance. Therefore, controlling the safety of the head vehicle was the key to ensuring the safety of the entire train when crosswinds were present at the tunnel entrance.

Finally, when the train entered the tunnel under crosswinds with different wind directions, the side forces of the head vehicle and the rear vehicle and the lift force of the head vehicle were most affected by the crosswinds. Furthermore, regardless of the directions of the crosswinds, the aerodynamic performance of the head vehicle was the worst, and its risk of overturning or derailment was the highest.

The aerodynamic loads acting on vehicles are affected by many factors, including the train speed, wind speed, yaw angle of the crosswinds, tunnel type, and shape of the train. To understand the aerodynamic performances of trains comprehensively, these factors need to be investigated in depth. Furthermore, the aerodynamic performances of trains running in special infrastructure scenarios, such as tunnels connecting bridges and tunnels connecting embankments under crosswinds, need to be further explored.

CRediT authorship contribution statement

Jianjun Luo: Conceptualization, Methodology, Supervision. **Lei Wang:** Conceptualization, Methodology, Investigation, Numerical calculation, Data analysis, Writing – original draft. **Suying Shang:** Verification, Visualization. **Feilong Li:** Visualization, Data management. **Dilong Guo:** Model test guidance. **Liping Gao:** Commenting, Reviewing. **Dengke Wang:** Reviewing.

Declaration of competing interest

The authors declare that they have no known competing financial interests or personal relationships that could have appeared to influence the work reported in this paper.

Data availability

No data was used for the research described in the article.

Acknowledgments

The authors gratefully acknowledge the support of the National Natural Science Foundation of China under Grants No. 51878038 and 51678036. The authors thank the anonymous reviewers who provided valuable suggestions that improved the manuscript.

References

Ali, I., Rüter, A., Ahlert, C.R., 2016. Numerical investigation on the embankment configuration for cross wind stability of ICE3. J. Appl. Comput. Mech. 8, 5–98.

Baker, C.J., 1985. The determination of topographical exposure factors for railway embankments. J. Wind Eng. Ind. Aerodyn. 21, 89–99.

Baker, C., 2009. Cross-wind effects on road and rail vehicles. Veh. Syst. Dyn. 47 (8), 983–1022.

Baker, C.J., 2010. The simulation of unsteady aerodynamic cross wind forces on trains. J. Wind Eng. Ind. Aerodyn. 98, 88–99.

BS EN14067-6, (2018). Railway applications - aerodynamics part 6: Requirements and test procedures for cross wind assessment.

CEN, 14067-3, 2003. European Standard Railway Applications – Aerodynamics – Part 3:Aerodynamics in Tunnels. CEN, Brussels.

Cheli, F., Corradi, R., Rocchi, D., Tomasini, G., Maestrini, E., 2010. Wind tunnel tests on train scale models to investigate the effect of infrastructure scenario. J. Wind Eng. Ind. Aerodyn. 98, 353–362.

Chen, Z., Liu, T., Yu, M., Chen, G., Chen, M., Guo, Z., 2020. Experimental and numerical research on wind characteristics affected by actual mountain ridges and windbreaks: A case study of the lanzhou-xinjiang high-speed railway. Eng. Appl. Comput. Fluid Mech. 14, 1385–1403.

Chen, Z., Liu, T., Zhou, X., Niu, J., 2017. Impact of ambient wind on aerodynamic performance when two trains intersect inside a tunnel. J. Wind Eng. Ind. Aerodyn. 169, 139–155.

Chu, C., Chien, S., Wang, C., Wu, T., 2014. Numerical simulation of two trains intersecting in a tunnel. Tunn. Undergr. Space Technol. 42 (5), 161–174.
Cooper, R.K., 1980. The probability of trains overturning in high winds. Wind Eng. 2, 1185–1194.
Cooper, R.K., 1981. The effect of cross-winds on trains. J. Fluid Eng. 103 (1), 170–178.
Copley, J.M., 1987. The three-dimensional flow around railway trains. J. Wind Eng. Ind. Aerodyn. 26 (1), 21–52.
Diedrichs, B., Sima, M., Orellano, A., Tengstrand, H., 2007. Crosswind stability of a high-speed train on a high embankment. Proc. Inst. Mech. Eng. 221, 205–225.
Ford, S.E., Riskowski, G., 2003. Effect of windbreak wall location on ventilation fan performance. Appl. Eng. Agric. 19, 343–346.
Guo, Z., Liu, T., Chen, Z., Liu, Z., Monzer, A., Sheridan, J., 2020. Study of the flow around railway embankment of different heights with and without trains. J. Wind Eng. Ind. Aerodyn. 202, 104203.
Guo, Z., Liu, T., Yu, M., Chen, Z., Li, W., Huo, X., Liu, H., 2019. Numerical study for the aerodynamic performance of double unit train under crosswind. J. Wind Eng. Ind. Aerodyn. 191, 203–214.
He, K., Gao, G., Wang, J., Fu, M., Miao, X., Zhang, J., 2018. Performance of a turbine driven by train-induced wind in a tunnel. Tunn. Undergr. Space Technol. 82, 416–427.
Hemida, H., Krajnović, S., 2009. Exploring flow structures around a simplified ICE2 train subjected to a 30° side wind using LES. Eng. Appl. Comput. Fluid Mech. 3, 28–41.
Hemida, H., Krajnović, S., 2010. LES study of the influence of the nose shape and yaw angles on flow structures around trains. J. Wind Eng. Ind. Aerodyn. 98, 34–46.
Horvat, M., Bruno, L., Khris, S., Raffaele, L., 2020. Aerodynamic shape optimization of barriers for windblown sand mitigation using CFD analysis. J. Wind Eng. Ind. Aerodyn. 197, 104058.
Jiang, Z., Liu, T., Chen, X., Li, W., Guo, Z., Niu, J., 2019. Numerical prediction of the slipstream caused by the trains with different marshalling forms entering a tunnel. J. Wind Eng. Ind. Aerodyn. 189, 276–288.
Khayrullina, A., Blocken, B., Janssen, W., Straathof, J., 2015. CFD simulation of train aerodynamics: Train-induced wind conditions at an underground railroad passenger platform. J. Wind Eng. Ind. Aerodyn. 139, 100–110.
Khier, W., Breuer, M., Durst, F., 2000. Flow structure around trains under side wind conditions: A numerical study. Comput. & Fluids 29, 179–195.
Li, W., Liu, T., Huo, X., Chen, Z., Guo, Z., Li, L., 2019. Influence of the enlarged portal length on pressure waves in railway tunnels with cross-section expansion. J. Wind Eng. Ind. Aerodyn. 190, 10–22.
Liu, D., 2019. Effect of wind speed variation on the dynamics of a high-speed train. Veh. Syst. Dyn. 57, 247–268.
Liu, T.H., Chen, Z.W., Chen, X.D., et al., 2017. Transient loads and their influence on the dynamic responses of trains in a tunnel. Tunn. Undergr. Space Technol. 66, 121–133.
Liu, T., Chen, Z., Zhou, X., Zhang, J., 2018. A CFD analysis of the aerodynamics of a high-speed train passing through a windbreak transition under crosswind. Eng. Appl. Comput. Fluid Mech. 12, 137–151.
Liu, T., Jiang, Z., Li, W., Guo, Z., Chen, X., Chen, Z., Krajnovic, S., 2019. Differences in aerodynamic effects when trains with different marshalling forms and lengths enter a tunnel. Tunn. Undergr. Space Technol. 84, 70–81.
Menter, F.R., 1994. Two-equation eddy-viscosity turbulence models for engineering applications. AIAA J. 32, 1598–1605.
Miao, X., Gao, G., 2015. Influence of ribs on train aerodynamic performances. J. Cent. South Univ. 22, 1986–1993.
Miao, X., He, K., Minelli, G., Zhang, J., Gao, G., Wei, H., He, M., Krajnovic, S., 2020. Aerodynamic performance of a high-speed train passing through three standard tunnel junctions under crosswind. Appl. Sci. Basel 10, 3664.
Miao, X.J., Zhang, L., Li, Z.W., Gao, G.J., Zeng, X.H., 2014. Aerodynamic performance of train passing out tunnel under cross-wind. J. Cent. South Univ. Sci. Technol. 45, 958–964 (in Chinese).
Montenegro, P.A., Heleno, R., Carvalho, H., Calçada, R., Baker, C.J., 2020. A comparative study on the running safety of trains subjected to crosswind simulated with different wind models. J. Wind Eng. Ind. Aerodyn. 207, 104398.
Niu, J., Sui, Y., Yu, Q., Cao, X., Yuan, Y., 2020. Aerodynamics of railway train/tunnel system: A review of recent research. Energy Built Environ. 1, 351–375.
Niu, J., Zhou, D., Liang, X., Liu, T., Liu, S., 2017a. Numerical study on the aerodynamic pressure of a metro train running between two adjacent platforms. Tunn. Undergr. Space Technol. 65, 187–199.
Niu, J., Zhou, D., Liang, X., Liu, S., Liu, T., 2018. Numerical simulation of the Reynolds number effect on the aerodynamic pressure in tunnels. J. Wind Eng. Ind. Aerodyn. 173, 187–198.
Niu, J., Zhou, D., Liu, T., Liang, X., 2017b. Numerical simulation of aerodynamic performance of a couple multiple units high-speed train. Veh. Syst. Dyn. 55, 681–703.
Ricco, P., Baron, A., Molteni, P., 2007. Nature of pressure waves induced by a high-speed train travelling through a tunnel. J. Wind Eng. Ind. Aerodyn. 95 (8), 781–808.
Rocchi, D., Tomasini, G., Schito, P., Somaschini, C., 2018. Wind effects induced by high speed train pass-by in open air. J. Wind Eng. Ind. Aerodyn. 173, 279–288.
Sun, Z., Dai, H., Gao, H., Li, T., Song, C., 2019. Dynamic performance of high-speed train passing windbreak breach under unsteady crosswind. Veh. Syst. Dyn. 57 (3), 408–424.
Suzuki, M., Tanemoto, K., Maeda, T., 2003. Aerodynamic characteristics of train/vehicles under cross winds. J. Wind Eng. Ind. Aerodyn. 91, 209–218.
Takanobu, O., Kozo, F., 1997. Numerical investigation of three-dimensional compressible flows induced by a train moving into a tunnel. Comput. & Fluids 26, 565–585.
Tomasini, G., Giappino, S., Corradi, R., 2014. Experimental investigation of the effects of embankment scenario on railway vehicle aerodynamic coefficients. J. Wind Eng. Ind. Aerodyn. 131, 59–71.
Wang, S.B., Bell, J.R., Burton, D., Herbst, A.H., Sheridan, J., Thompson, M.C., 2017. The performance of different turbulence models (URANS, SAS and DES) for predicting high-speed train slipstream. J. Wind Eng. Ind. Aerodyn. 165, 46–57.
Wang, M., Li, X., Xiao, J., Sha, H., Zou, Q., 2020. Effects of infrastructure on the aerodynamic performance of a high-speed train. Proc. Inst. Mech. Eng. 1791156491.
Wang, T., Wu, F., Yang, M., Ji, P., Qian, B., 2018. Reduction of pressure transients of high-speed train passing through a tunnel by cross-section increase. J. Wind Eng. Ind. Aerodyn. 183, 235–242.
Xiang, X.T., Xue, L.P., 2010. Tunnel hood effects on high speed train-tunnel compression wave. J. Hydrodyn. Ser. Bull. 22 (5), 940–947.
Yang, W., Deng, E., Lei, M., Zhu, Z., Zhang, P., 2019. Transient aerodynamic performance of high-speed trains when passing through two windproof facilities under crosswinds: A comparative study. Eng. Struct. 188, 729–744.
Yang, Q., Song, J., Li, D., Zhang, J., Yang, G., 2013. Train model acceleration and deceleration. Sci. China Technol. Sci. 56, 642–647.
Yang, Q., Song, J., Yang, G., 2016. A moving model rig with a scale ratio of 1/8 for high speed train aerodynamics. J. Wind Eng. Ind. Aerodyn. 152, 50–58.
Yao, S.B., Guo, D.L., Sun, Z.X., Chen, D.W., Yang, G.W., 2016. Parametric design and optimization of high speed train nose. Optim. Eng. 17, 605–630.
Yao, S., Guo, D., Sun, Z., Yang, G., Chen, D., 2014. Optimization design for aerodynamic elements of high speed trains. Comput. & Fluids 95, 56–73.

Yao, Z., Zhang, N., Chen, X., Zhang, C., Xia, H., Li, X., 2020. The effect of moving train on the aerodynamic performances of train-bridge system with a crosswind. Eng. Appl. Comput. Fluid Mech. 14, 222–235.
Zhang, J., Gao, G., Liu, T., Li, Z., 2015. Crosswind stability of high-speed trains in special cuts. J. Cent. South Univ. 22, 2849–2856.
Zhang, L., Liu, H., Stoll, N., Thurow, K., 2017. Influence of tunnel aerodynamic effects by slope of equal-transect ring oblique tunnel portal. J. Wind Eng. Ind. Aerodyn. 169, 106–116.
Zhang, J., Zhang, M., Li, Y., Fang, C., Xiang, H., 2019. Wind tunnel test study on complex wind field and vehicle aerodynamic effects in embankment-cutting transition zone in high-speed railway. Eng. Mech. 36 (1), 80–87, (in Chinese).
Zhou, X., Liu, T., Chen, Z., Zou, X., Liu, D., 2017. Effect of ambient wind on pressure wave generated by high-speed train entering a tunnel. J. Cent. South Univ. 24, 1465–1475.
Zhuang, Y., Lu, X., 2015. Numerical investigation on the aerodynamics of a simplified high-speed train under crosswind. Theor. Appl. Mech. Lett. 5, 181–186.